ADVANCED FUNCTIONAL MATERIALS
www.afm-journal.de

Self-Pumped Hygroscopic Nanofiber Emitter for Ozone-Free Water Electrospray-Based Air Purification

Jihwan Chae, Yujang Cho, Jiyeon Yu, Sungyoon Woo, Seongcheol Ahn, Changhoon Ahn, Mingyu Sagong, Euichul Shin, Jinyoung Choi, Seung S. Lee, and Il-Doo Kim**

Indoor air purification technologies encounter inherent trade-offs among efficiency, safety, and scalability. Conventional filter-based systems are hindered by increasing pressure drop and frequent maintenance, whereas filterless electrostatic precipitators produce hazardous ozone due to corona discharge and demand high operating voltages. Here, a compact ozone-free air purification system is demonstrated, which utilizes water electrospray driven by a self-pumped hygroscopic nanofiber emitter. The emitter comprises an electrospun organic–inorganic composite membrane of poly(vinyl alcohol), poly(acrylic acid), and montmorillonite. This hybrid structure integrates the hygroscopic and chemically active properties of the polymers with the mechanical reinforcement of the inorganic filler, enabling continuous capillary-driven water transport. The hygroscopic emitter autonomously transports water to the emission tip, enabling stable cone-jet electrospray without external pumps. A ring-shaped extractor electrode concentrates the local electric field, thereby sustaining water electrospray below 5 kV. In a 0.1 m^3 sealed chamber, the device achieves over 97% removal of $PM_{0.3}$ within 5 min across 30 repeated operation cycles, while maintaining ozone levels below 20 ppb and water consumption under 0.4 mL h^{-1} per emitter tip. These results establish hygroscopic nanofiber-based electrospray emitters as a safe, energy-efficient, and scalable platform for filterless indoor air purification.

1. Introduction

Indoor air pollution, encompassing fine particulate matter (PM), volatile organic compounds (VOCs), and microbial aerosols, is a critical contributor to respiratory, cardiovascular, and neurological diseases.[1,2] Traditional mitigation strategies predominantly rely on high-efficiency particulate air (HEPA) filters, which mechanically entrap airborne particulates on fibrous media as air flows through. Although effective, HEPA filters progressively accumulate particulates, resulting in increased pressure drop, diminished airflow, and the need for frequent replacement.[3,4] As a filterless alternative, electrostatic precipitators (ESPs) charge aerosols and collect them on plates with minimal pressure drop and extended operational life. However, their efficiency diminishes markedly for submicron aerosols due to inherently low charge-to-mass ratios, and particle re-entrainment often occurs under high flow or vibration conditions.[5,6] To overcome these limitations, wet ESPs (WESPs) have been developed, wherein a thin water film on the collection plates enhances particle adhesion and suppresses re-entrainment.[7–9] Nonetheless, both ESPs and WESPs employ high voltage (HV) corona discharge for ion generation, inadvertently producing ozone,[7,10] a hazardous indoor pollutant with well-documented health risks.[11] Moreover, WESPs require bulky infrastructure, continuous water supply, and substantial power input, rendering them impractical for compact or water-sensitive indoor environments.

Electrospray-based air purification system offers a promising alternative to conventional air purification methods. This approach involves applying a high electric field to a liquid via a fine nozzle, resulting in the emission of highly charged microdroplets, a phenomenon known as electrospray. These microdroplets capture airborne particles through electrostatic interaction and inertial impaction, enabling efficient removal without intentional ozone generation.[12–14] Electrospray can operate in various regimes, such as dripping, spindle, and cone-jet, depending on the nozzle geometry, applied voltage, flow rate, and fluid properties.[15] Among these regimes, the cone-jet mode is particularly advantageous. When electrostatic and surface tension forces are balanced, a cone-shaped liquid interface, known

J. Chae, S. S. Lee
Department of Mechanical Engineering
Korea Advanced Institute of Science and Technology (KAIST)
291 Daehak-ro, Yuseong-gu, Daejeon 34141, Republic of Korea
E-mail: sslee97@kaist.ac.kr
Y. Cho, S. Woo, S. Ahn, C. Ahn, M. Sagong, E. Shin, I.-D. Kim
Department of Materials Science and Engineering
Korea Advanced Institute of Science and Technology (KAIST)
291 Daehak-ro, Yuseong-gu, Daejeon 34141, Republic of Korea
E-mail: idkim@kaist.ac.kr
J. Yu, S. S. Lee
A2US Corporation
247 Yangji-ro, Bucheon 14786, Republic of Korea
J. Choi
Division of Future Energy Technology
Dongshin University
Naju 58245, Republic of Korea

The ORCID identification number(s) for the author(s) of this article can be found under https://doi.org/10.1002/adfm.202523456

DOI: 10.1002/adfm.202523456

as a Taylor cone, forms and emits a fine, stable jet. This jet produces highly charged and monodisperse microdroplets that are much smaller than the nozzle diameter.[16,17] These droplets typically evaporate during flight, enabling quasi-dry operation with minimal liquid usage, while effectively capturing submicron aerosols.[14] Additionally, water electrospray in the cone-jet mode has been shown to generate reactive oxygen species (ROS), including hydroxyl radicals, which inactivate airborne bacteria and viruses without the need for chemical additives.[18,19] Furthermore, recent studies have demonstrated that dielectric-interface engineering, such as the introduction of polydopamine-modified fibrous membranes, can significantly enhance charge stability and particle adhesion under high-velocity airflow while maintaining ozone-free operation, highlighting the potential of interfacial polarization control in electrohydrodynamic air-purification systems.[20]

Despite these benefits, cone-jet water electrospray remains technically challenging due to the high surface tension and electrical conductivity of water, which necessitate high onset voltages and often trigger undesirable corona discharge.[15,21,22] To address these fluid property limitations, alcohol-water mixtures such as ethanol and methanol have been used to lower surface tension and facilitate stable electrospray at reduced voltages.[12–14,23,24] However, their volatility and potential health hazard constrain their use in indoor environments. Alternatively, dielectric micronozzles fabricated from ceramic,[22] polymer,[25] or silicon-based materials.[26] have been employed to intensify the local electric field and suppress discharge. While effective, these devices are often costly, prone to clogging, and difficult to mass-produce.

Recently, self-pumped emitters composed of porous materials have emerged as a promising structural solution, leveraging capillary action to transport water passively to the nozzle tip without the need for external pumps.[12,27,28] These emitters operate without external pumps by using porous materials that continuously draw and replenish water via capillary action. This self-pumped design simplifies the system and enhances reliability by minimizing mechanical components and operating without nozzle clogging. Nevertheless, long-term stability remains limited by inconsistent wetting and material degradation. Most self-pumped emitters use cellulose filter paper for its low cost and inherent wettability, yet repeated wet–dry cycling causes swelling, warping, and delamination that erode dimensional fidelity and destabilize cone-jet water electrospray.[28] The large exposed porous area also promotes evaporation, reducing the effective supply to the emission zone and amplifying device-to-device variability.[28] These limitations motivate material-level designs that retain capillary feed while improving durability and evaporation control. Along similar lines, recent developments in biodegradable dielectric fibrous membranes have highlighted that well-designed polymer–inorganic interfaces can simultaneously ensure efficient particle capture and mechanical stability under continuous operation.[29] Inspired by these advances, this study introduces a self-pumped hygroscopic nanofiber emitter that autonomously supplies water while maintaining a stable cone-jet mode for ozone-free, long-term air purification.

We developed a hybrid organic–inorganic nanofiber composite emitter that is a crosslinked polyvinyl alcohol (PVA)-polyacrylic acid (PAA) network reinforced with montmorillonite (MMT), forming a hygroscopic nanofiber membrane encapsulated in a laminated polyimide (PI)/polyethylene terephthalate (PET) microchannel that exposes only the sharpened tip. This architecture couples the hydrophilicity and chemical functionality of the polymer matrix with the mechanical robustness and dimensional stability of the inorganic filler, such as MMT, sustaining capillary water transport while resisting swelling and delamination under wet–dry cycling. By suppressing lateral wicking and evaporation, the laminated channel concentrates feed at the emission zone, enabling stable cone-jet water electrospray with minimal liquid use and improved long-term reliability. Building upon prior work on self-pumped emitters,[27,28] this study presents a compact, filterless air purification device that utilizes ozone-free cone-jet water electrospray, facilitated by a self-pumped hygroscopic nanofiber emitter. As schematically illustrated in **Figure 1**, the system comprises a water reservoir, a nanofiber-based capillary structure, a four-tip emitter, a high-voltage (HV) module, a grounded particle collector, and an integrated air-circulating fan, all housed in a cylindrical enclosure. Charged water microdroplets generated by cone-jet water electrospray at the emitter tip are directed toward the grounded collector, enabling efficient particle capture. The hygroscopic nanofiber membrane is fabricated by electrospinning a hydrophilic polymer with MMT onto a conductive substrate. A ring-shaped extractor concentrates the local electric field to stabilize cone-jet water electrospray and suppress corona discharge during operation.

2. Results and Discussion

2.1. Self-Pumped Hygroscopic Nanofiber-Based Electrospray Emitter

Figure 2 illustrates the fabrication process and structural characterization of an organic–inorganic composite nanofiber membrane designed to serve as a self-pumped water emitter. As shown in Figure 2a, a homogeneous solution containing PVA, PAA, and MMT was subjected to electrospinning under a high electric field, resulting in the formation of a PVA-PAA-MMT nanofiber membrane (PPM-NFM). During jet elongation and solidification stages, the polymer chains and dispersed inorganic nanofillers are directionally aligned in a co-axial nanostructure, and when a high voltage field is applied, the MMT migrates toward the outer layer of the nanofiber due to the hydroxyl groups on its surface.[30] This arrangement facilitates the formation of a continuous porous network capable of efficient capillary-driven water transport.[31,32] To improve water resistance and mechanical robustness, the as-spun membrane underwent thermal treatment at 150 °C for 3 h. Under these conditions, an esterification reaction occurs between the hydroxyl groups of PVA and the carboxylic acid groups of PAA,[33,34] as illustrated in Figure 2b:

$$-\mathrm{OH\ (PVA)} + -\mathrm{COOH\ (PAA)} \rightarrow -\mathrm{COO} - + \mathrm{H_2O} \quad (1)$$

This esterification reaction resulted in the formation of covalent ester bonds, establishing a chemically crosslinked polymer network with significantly enhanced structural integrity.[35,36] The resulting composite exhibited markedly improved mechanical strength, chemical resistance, and water repellency, all of which are essential for the sustained operation of electrospray

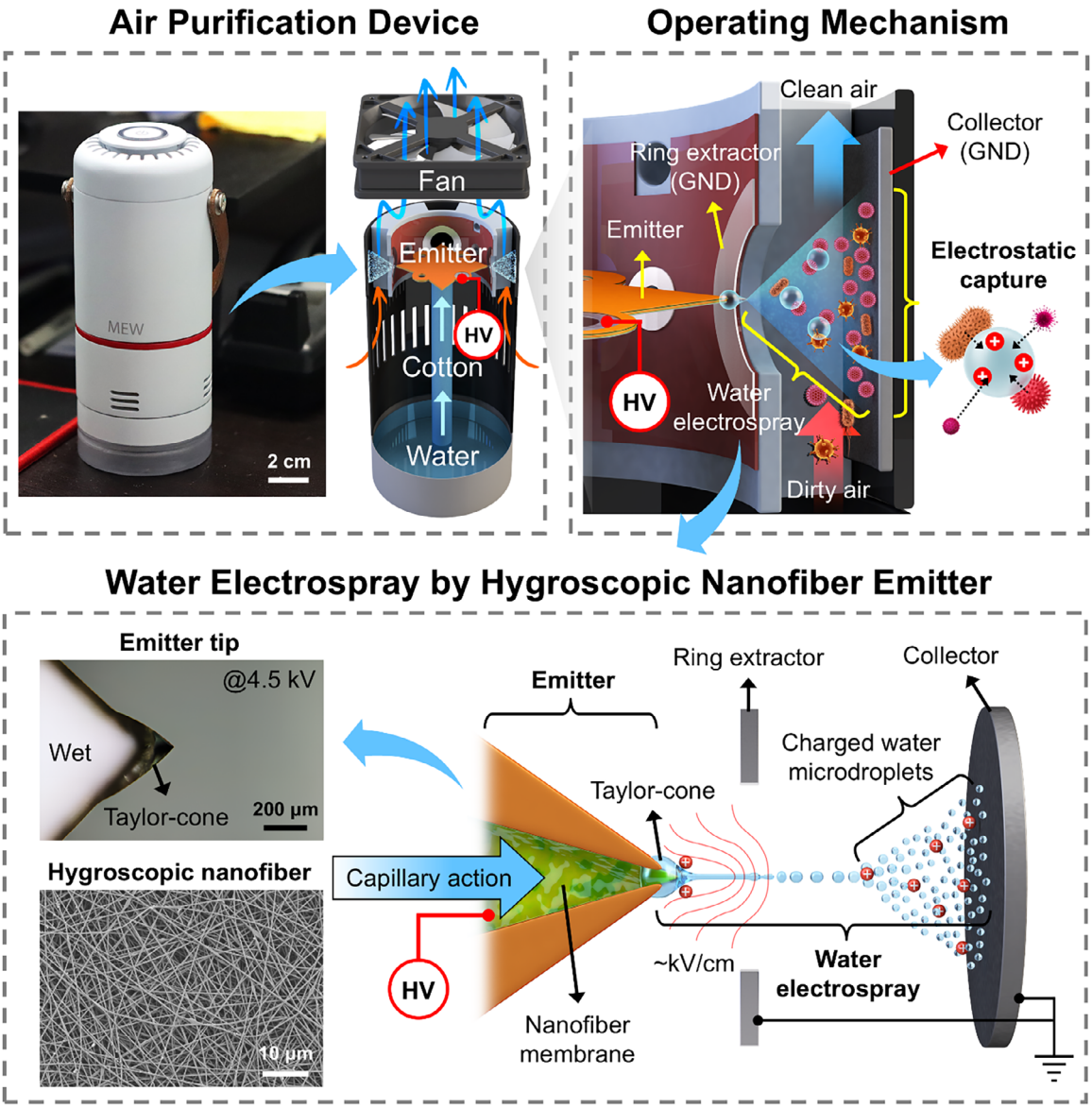

Figure 1. Design and operating mechanism of a compact air purification device based on cone-jet water electrospray using a self-pumped hygroscopic PVA-PAA-MMT nanofiber membrane (PPM-NFM) emitter.

systems under ambient conditions. Beyond chemical crosslinking, the incorporation of MMT further reinforced the composite architecture. MMT is a 2:1 phyllosilicate characterized by negatively charged lamellar layers and an interlayer space capable of hosting hydrated cations and water molecules.[37,38] These features confer a strong affinity for polar species, and when uniformly dispersed within the polymer matrix, MMT contributes not only to mechanical reinforcement but also to moisture retention. This effect is particularly enhanced when MMT is intercalated with sodium (Na^+) ions, which facilitate water sorption through cation hydration mechanisms.[39]

Figure 2c presents the stepwise fabrication of a multilayer electrospray PPM(PVA-PAA-MMT)-NFM emitter designed to integrate the previously described hygroscopic organic–inorganic materials. To ensure scalability and precise structural control, a flexible printed circuit board (FPCB) fabrication approach based on sequential 2D film lamination was employed. This method facilitates robust electrical insulation of the HV electrode and enables straightforward construction of high-aspect-ratio microchannels. In step (i), an 18 μm-thick copper (Cu) layer was laminated onto a 50 μm-thick PI substrate using a 10 μm-thick hot melt adhesive (omitted in the schematic), followed by hot pressing, photolithographic patterning, and wet etching. To prevent surface oxidation and maintain conductivity, a ≈2 μm-thick nickel (Ni) layer was deposited by electroless plating, forming a Cu/Ni electrode. In step (ii), a 300 μm-thick PI film was laser-cut to create a rectangular groove and laminated onto the base layer, defining the space for microchannel construction. In step (iii), the prefabricated hygroscopic PPM-NFM and an indium tin oxide (ITO)-coated film (total thickness ≈130 μm) were inserted into

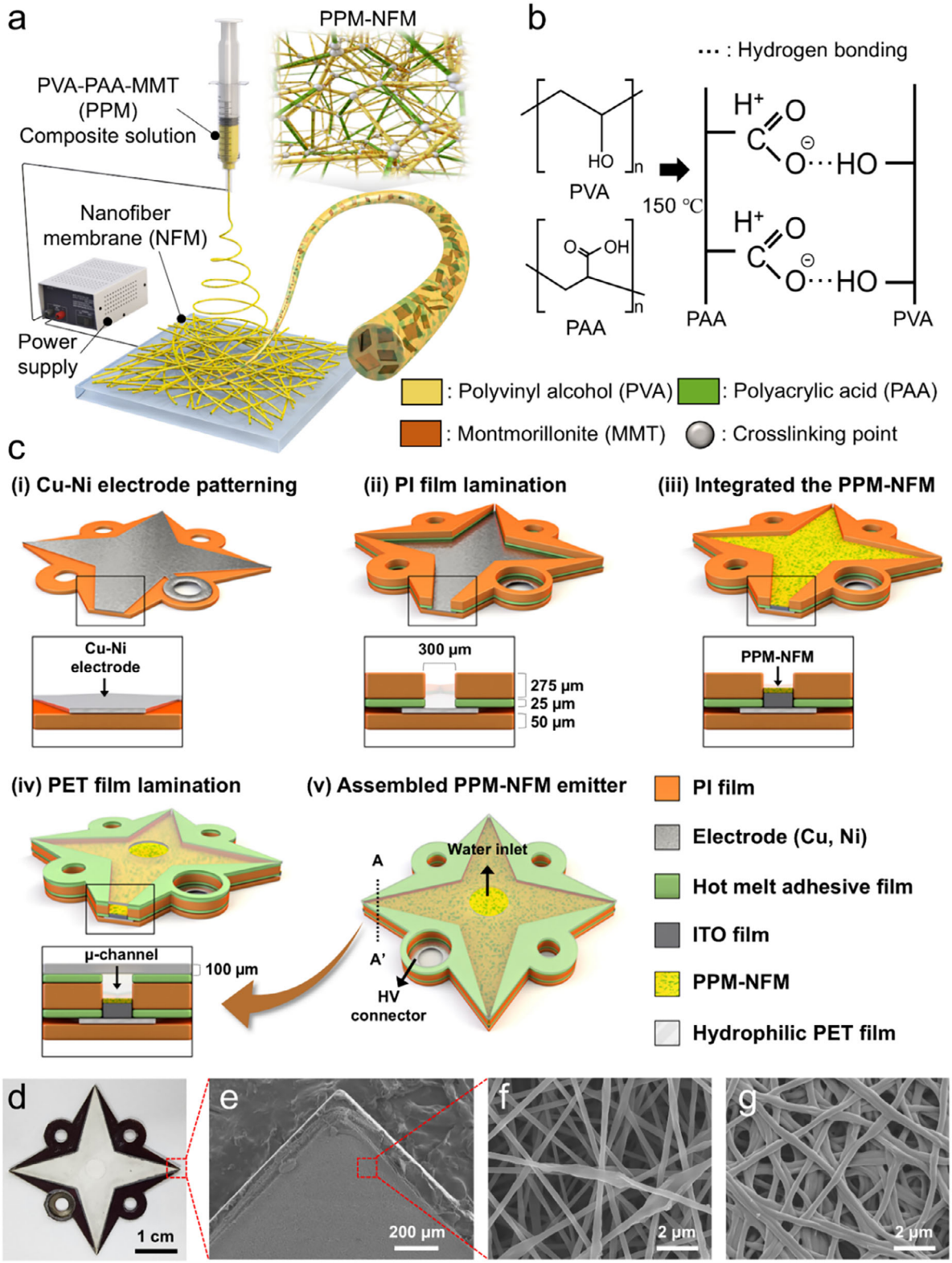

Figure 2. Fabrication and integration of the PPM-NFM into a self-pumped electrospray emitter. a) Schematic of the electrospinning setup for producing the PPM-NFM. b) Schematic illustration of the thermal crosslinking of PVA and PAA. c) Stepwise schematic of the multilayer emitter assembly including Cu/Ni electrode, microchannel, PPM-NFM, and sealing layers. d) Optical images of the emitter and PPM-NFM. e) SEM image of the emitter tip showing sharp geometry. f–g) SEM images of the PPM-NFM surface: (f) as-spun nanofiber morphology and g) morphology after immersion in water followed by drying, showing structural stability.

the groove, serving as the core functional emitter layer. In step (iv), a hydrophilic PET film with a pre-formed central water inlet was laminated to seal the structure. Consequently, a lateral microchannel with an approximate cross-section of 300 × 200 μm^2 was formed, enabling stable water delivery to the emitter tip. The individual components used in the multilayer assembly process, including the Cu/Ni-plated PI film (base electrode), the PPM-NFM (functional emitter layer), and the PET film (top sealing layer), are shown in Figure S1 (Supporting Information). In step (v), the fully assembled emitter is shown, with the hygroscopic PPM-NFM exposed at the tip region. As shown in Figure 2d, the PPM-NFM emitter tip has a half-angle of ≈45°, which is close to the theoretical Taylor cone angle of 49.3°,[16] thereby providing a favorable geometry for stable cone-jet water electrospray. An HV connector is exposed on the emitter surface for connection to the HV module. To evaluate the practical applicability of the membrane, a custom-designed, star-shaped four-tip emitter was fabricated, as illustrated in Figure 2d. Surface scanning electron microscopy (SEM) imaging confirmed the successful incorporation of PPM-NFM as the core functional layer within the emitter architecture (Figure 2e). High-magnification SEM images (Figure 2f) revealed a uniform fibrous morphology, with the presence of MMT promoting surface roughness and the formation of interfiber junctions. These features suggest enhanced mechanical interlocking and synergistic reinforcement within the composite nanofiber networks. Moreover, the thermal crosslinking process contributed to preserving nanofiber integrity, particularly under hydrated conditions. To validate the effectiveness of the crosslinking strategy, the membrane was immersed in deionized (DI) water and subsequently dried. As shown in Figure 2g, SEM images were obtained after immersing the PPM-NFM in 1 mL of DI water, followed by drying in a vacuum oven at 60 °C for 10 h. In contrast, the non-crosslinked PVA/PAA-NFM rapidly dissolved upon DI water exposure, as evidenced in Figure S2 (Supporting Information), underscoring the indispensable role of thermal crosslinking in enabling long-term, water-stable operation of the self-pumped PPM-NFM emitter.

2.2. Thermal Crosslinking and Capillary Performance of PPM-NFM Emitters

Figure 3a displays a cryo-TEM micrograph of a single PPM-NFM incorporating MMT nanosheets. The low-temperature imaging clearly reveals that the layered MMT platelets are uniformly embedded and well aligned along the nanofiber axis, without any evidence of aggregation or phase separation. The inset shows the fast Fourier transform (FFT) pattern, which exhibits a periodic lattice spacing of ≈0.5 nm, corresponding to the (002) reflection of montmorillonite, consistent with a basal (001) spacing of ≈1.0 nm in exfoliated MMT layers (Figure S3, Supporting Information). This observation confirms that the nanosheets retain their layered crystalline structure and are finely dispersed within the PVA–PAA matrix. Complementary structural information was obtained from the focused ion beam–scanning electron microscopy (FIB-SEM) analysis shown in Figure 3b, which presents a cross-sectional view of the nanofiber mat exhibiting a densely entangled and continuous fibrous network with no apparent filler agglomeration. The accompanying energy-dispersive spectroscopy (EDS) elemental maps (Figure 3c–g) further verify the homogeneous distribution of inorganic elements (C, O, Si, Na, and Al) throughout the composite membrane. The uniform spatial distribution of these elements across the entire cross-section demonstrates that MMT is evenly dispersed within the nanofibers, forming a well-interconnected nanofiller network. Collectively, these structural characterizations confirm that the MMT nanosheets are uniformly integrated within the polymer matrix, thereby facilitating efficient interfacial load transfer and enhancing the overall structural integrity of the PPM-NFM composite (Figure S4, Supporting Information).

The thermal crosslinking behavior of the PPM-NFM was systematically investigated using Fourier Transform Infrared (FT-IR) spectroscopy, as shown in Figure 3h. Following thermal treatment at 150 °C for 3 h, distinct spectral changes were observed, confirming the occurrence of esterification reactions between the hydroxyl groups of PVA and the carboxylic acid groups of PAA.[40] Notably, the broad O—H stretching band centered ≈3300 cm^{-1} exhibited a substantial decrease in intensity, reflecting the consumption of hydroxyl groups during ester bond formation. Concurrently, an absorption peak emerged at ≈1720 cm^{-1}, attributed to the carbonyl (C═O) stretching of ester linkages.[41] The position of this carbonyl peak, which appears at a slightly lower wavenumber than typical ester peaks (≈1735–1750 cm^{-1}), can be attributed to strong hydrogen bonding interactions and restricted chain mobility within the polymer matrix.[42] The presence of MMT is likely to contribute to this shift by influencing local chain mobility and interfacial interactions. In addition, an increased signal near 1040 cm^{-1}, associated with asymmetric C—O—C stretching vibrations, provides additional evidence for successful ester bond formation. No new peaks corresponding to MMT were observed, indicating that MMT remained chemically inert under thermal treatment conditions. Rather than participating in chemical reactions, MMT likely functioned as a physically reinforcing phase, offering structural support and enhancing the morphological stability of the nanofiber network.

To further elucidate the chemical evolution of the composite, high-resolution C 1s X-ray photoelectron spectroscopy (XPS) analysis was conducted before and after thermal treatment at 150 °C (Figure 3i). The C 1s spectra were deconvoluted into three primary components located at 284.8 eV (C—C), 286.0 eV (C—O), and 288.8 eV (O—C═O), corresponding to the carbon backbone and functional groups of PVA and PAA.[36] Following thermal crosslinking, the relative areas of the C—O and O—C═O species decreased from 0.59 to 0.46 and from 0.25 to 0.21, respectively. This reduction indicates the consumption of hydroxyl and carboxylic acid groups during ester bond formation. For comparison, a thermally treated control sample without MMT retained higher relative intensities for C—O (0.53) and O—C═O (0.25) peaks, suggesting a lower degree of crosslinking in the absence of the inorganic component (Figure S5, Supporting Information). These results imply that MMT not only contributes to mechanical reinforcement but may also facilitate the crosslinking reaction.[43] This enhancement may be attributed to the spatial confinement effect induced by MMT, which restricts polymer chain mobility and promotes proximity between reactive functional groups, thereby increasing the efficiency of esterification.

Figure 3j presents the tensile test results used to evaluate the mechanical performance of the PPM-NFM. The pristine

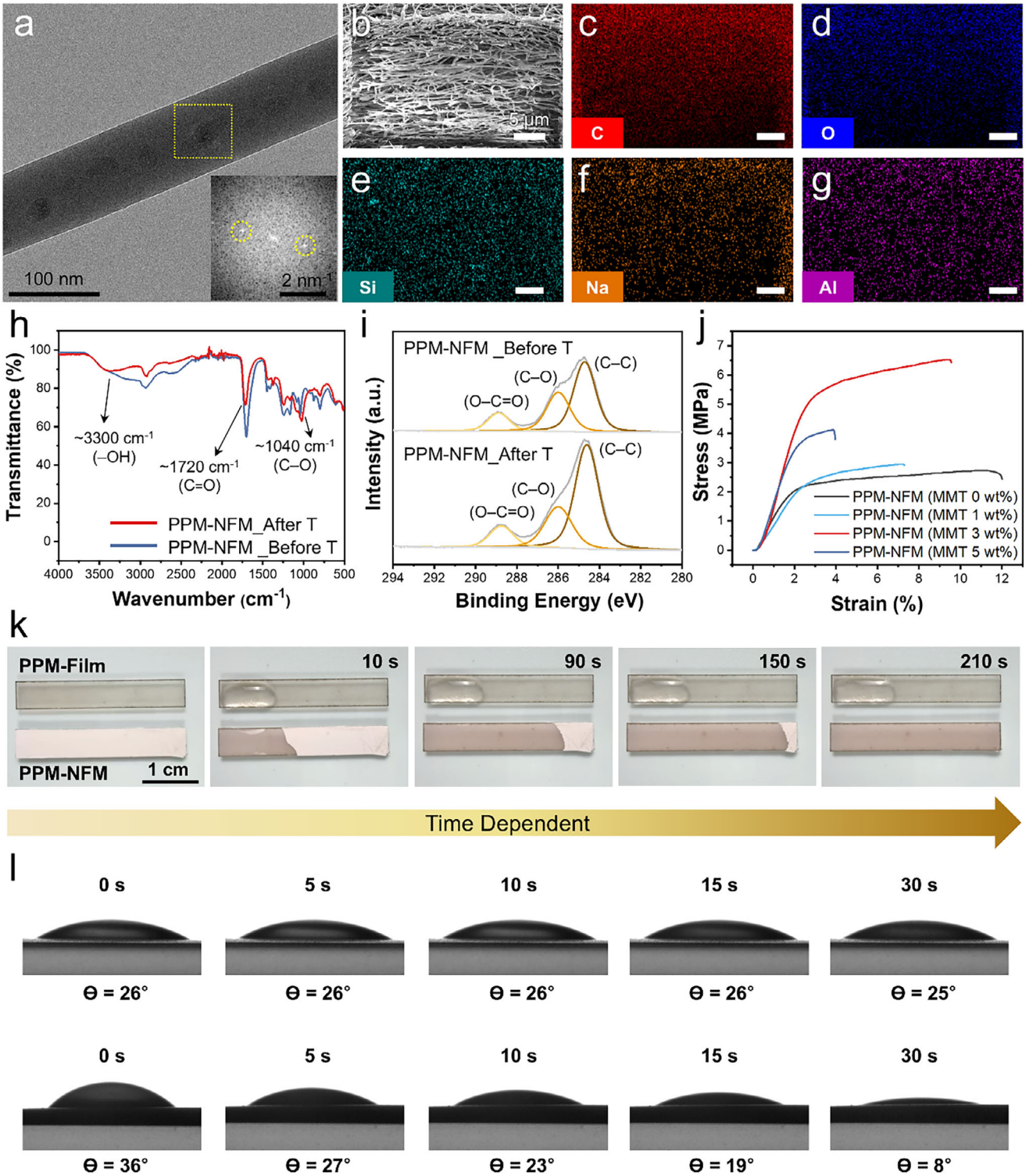

Figure 3. Physicochemical and functional characterization of the PPM-NFM. a) Cryo-TEM image showing uniformly dispersed MMT nanosheets within the nanofiber, with the inset FFT pattern confirming the layered structure of exfoliated MMT. b) FIB-SEM cross-sectional image displaying a continuous and densely entangled fibrous network structure. c–g) EDS elemental mapping images of C, O, Si, Na, and Al, confirming the homogeneous distribution of MMT components within the nanofiber matrix without noticeable aggregation or phase separation. h) FT-IR spectra confirming esterification between PVA and PAA after thermal treatment. i) C 1s XPS spectra before and after crosslinking, showing reduction in hydroxyl and carboxyl groups. j) Tensile performance of PPM-NFMs with varying MMT content (0, 1, 3, and 5 wt.%). k) Time-lapse images comparing water absorption of PPM film and PPM-NFM. l) Time-dependent contact angle measurements of PPM film (top) and PPM-NFM (bottom), demonstrating enhanced wettability and capillary-driven infiltration.

PVA/PAA membrane exhibited relatively low tensile strength (≈3.4 MPa) but achieved the highest elongation at break (≈11%), characteristic of its ductile nature. Upon incorporation of 1 wt.% MMT, the composite demonstrated a modest enhancement in tensile strength (≈4.2 MPa), accompanied by a slight decrease in elongation. This behavior is indicative of improved interfacial stress transfer between the polymer matrix and the exfoliated clay nanosheets.[30] Notably, the composite containing 3 wt.% MMT achieved the highest tensile strength (≈7.2 MPa) with a well-balanced elongation (≈8.5%), suggesting optimal nanoparticle dispersion and effective reinforcement through hydrogen bonding and physical interlocking within the nanofibrous network. Conversely, further increasing the MMT content to 5 wt.% resulted in diminished tensile strength (≈5.5 MPa) and reduced ductility (≈6%), likely due to nanoparticle agglomeration that compromises the matrix continuity and introduces stress concentration sites. Taken together, these results demonstrate that an MMT content of 3 wt.% provides an optimal balance between mechanical reinforcement and structural integrity, underscoring the critical role of nanoparticle dispersion and interfacial compatibility in enhancing the mechanical properties of PPM-NFM. This mechanical robustness, combined with the hygroscopic and capillary-active nature of the composite, renders the MMT-integrated PPM-NFM highly suitable for self-pumped operation in moisture-driven systems.

To investigate the water absorption performance relevant to self-pumped water emission, PPM composites were fabricated in both nanofiber (PPM-NFM) and film (PPM film) forms. Water absorption dynamics were real-time monitored by applying 20 µL of DI water to one end of each emitter (3 × 0.5 cm^2, with a thickness of 48 µm as determined from the FIB cross-sectional SEM analysis (Figure S6, Supporting Information). Despite their intrinsic hydrophilicity, PPM composite films showed negligible water spreading. This limited water spreading is attributed to their dense and uniform morphology, which restricts lateral diffusion, causing water to remain localized at the point of application. In contrast, the PPM-NFM exhibited continuous water uptake and directional diffusion along the membrane, driven by capillary action enabled by the fibrous architecture. This behavior was directly visualized by time-lapse video imaging (Movie S1, Supporting Information), as shown in Figure 3k.

To quantitatively validate these findings, contact angle measurements were conducted (Figure 3l). The PPM film exhibited a relatively stable contact angle of ≈25° over a 30-s period, indicative of limited wettability and constrained water spreading. In contrast, the PPM-NFM demonstrated a pronounced reduction in contact angle, from 36° to 8°, within the same time frame, signifying substantially enhanced wettability and dynamic water infiltration. Notably, despite its superior wetting behavior over time, the PPM-NFM initially presented a higher contact angle than the dense film by ≈10°, a phenomenon that can be ascribed to the Cassie–Baxter effect.[44] According to the Cassie–Baxter Equation (1):

$$\cos\theta_C = f_s \cos\theta_Y + f_v \cos\theta_v \quad (2)$$

where θ_C is the apparent contact angle in the Cassie state, f_s is the fractional area of the solid surface in contact with the liquid, and θ_Y is the intrinsic Young's contact angle on a flat solid surface. f_v represents the fractional area of trapped air beneath the liquid droplet, and θ_v is the contact angle on air, typically approximated as 180°, such that $\cos\theta_v = -1$. This effect arises from the presence of a porous and microstructured surface, which initially traps air pockets beneath the droplet, leading to an apparent increase in hydrophobicity prior to the collapse into a fully wet state. Over time, however, this structure enabled accelerated water infiltration, confirming the dynamic wetting behavior of the nanofiber-based emitter. These results demonstrate that the PPM-NFM possesses spontaneous water absorption and directional transport capabilities due to its capillary-active fibrous structure, making it a highly suitable platform for self-pumped emitter applications in moisture-driven systems.

2.3. Characterization of Cone-Jet Water Electrospray

The performance of the hygroscopic PPM-NFM emitter was evaluated using a custom-built test setup, as illustrated in **Figure 4a**. The PPM-NFM emitter was connected to an HV supply, while the collector was grounded to establish a stable electric field and facilitate the safe collection of charged water microdroplets. A grounded ring extractor was concentrically aligned with the PPM-NFM emitter tip to concentrate the local electric field at the tip, thereby reducing the onset voltage for electrospray and effectively suppressing corona discharge. DI water, exhibiting an electrical conductivity of 0.103 mS m^{-1}, was employed as the working fluid. The electrospray current, which originated from the convective transport of charge carried by the emitted droplets, was measured using a picoammeter. A high-speed camera equipped with light-emitting diode (LED) backlighting was also used to capture time-resolved images of the meniscus and jet dynamics at the PPM-NFM emitter tip.

Figure 4b presents the current–voltage (I—V) characteristics under three experimental conditions: (i) wet PPM-NFM emitter without ring extractor, (ii) wet PPM-NFM emitter with ring extractor, and (iii) dry PPM-NFM emitter with ring extractor. No measurable current was observed under conditions (i) and (iii), indicating that both a continuous water supply and appropriate electric field distribution via the ring extractor are essential for electrospray initiation. In contrast, under condition (ii), a distinct transition of electrospray modes was observed with increasing voltage. In the range of 4.1–4.2 kV, the PPM-NFM emitter operated in a dripping mode, where brief and unstable formation of Taylor cone intermittently allowed the emission of charged water microdroplets, which produced a small but measurable current. Upon increasing the voltage to 4.3–4.6 kV, the PPM-NFM emitter exhibited a near-constant current plateau, indicative of stable cone-jet mode operation.[22] The average current within this regime was 98.1 nA, confirming steady-state emission of charged water microdroplets. At voltages exceeding 4.7 kV, a sharp rise in current accompanied by visible discharge indicated the onset of corona discharge, thereby marking the upper voltage limit for stable cone-jet operation.

These transitions in electrospray behavior were visually confirmed by high-speed imaging, as shown in Figure 4c. In the dripping mode (Figure 4c(i)), the tip alternated between a rounded meniscus and a briefly emerging Taylor cone. In the cone-jet regime, a stable Taylor cone with continuous microjet emission

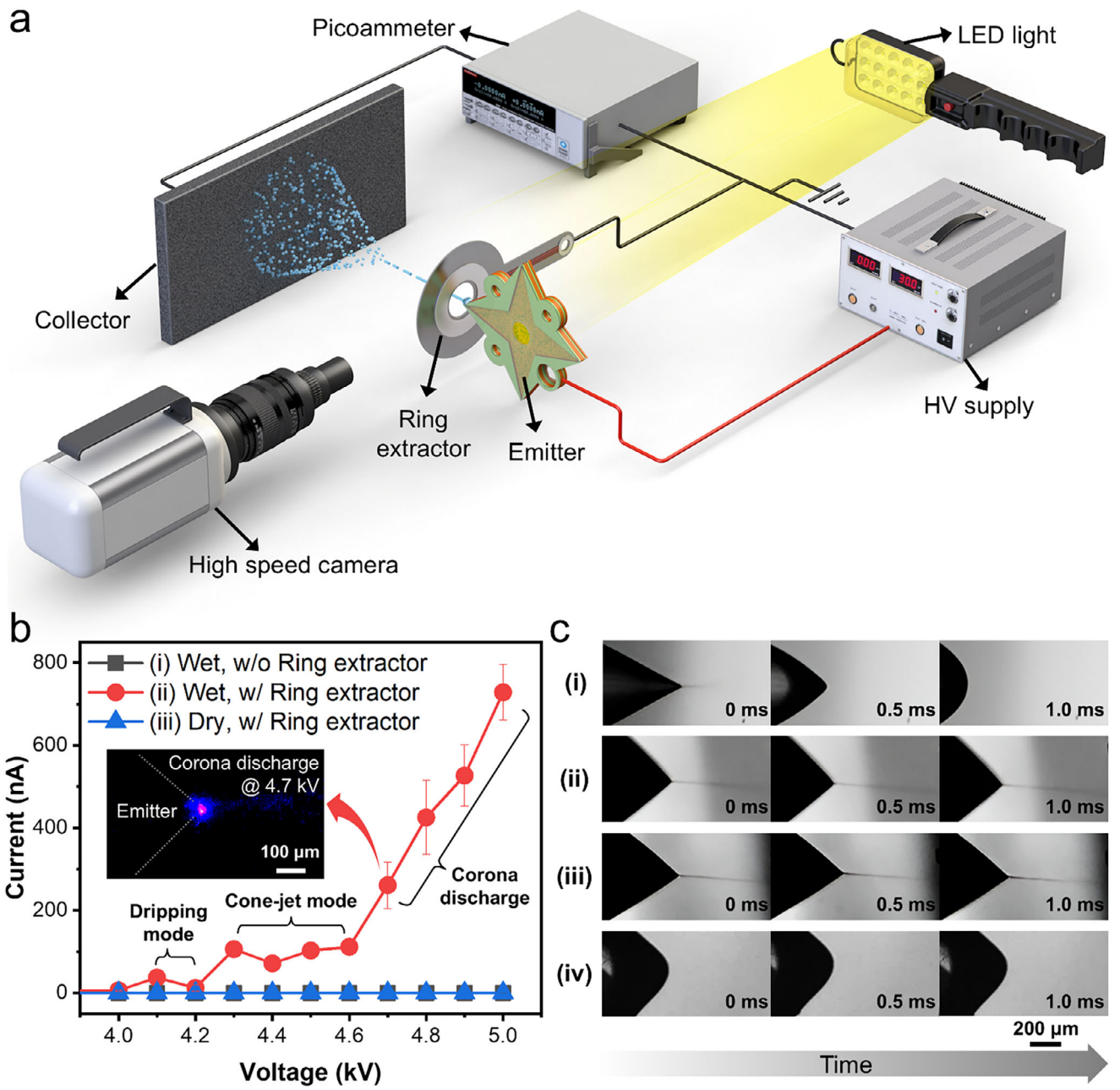

Figure 4. Experimental setup and characterization of cone-jet electrospray performance. a) Experimental setup for current measurement and high-speed imaging of water electrospray. b) I–V characteristics under three conditions showing stable cone-jet mode only with water and ring extractor; corona discharge occurs above 4.7 kV. The data are represented as mean ± SD (n = 100). c) High-speed images at representative voltages: (i) dripping (4.2 kV), (ii–iii) cone-jet (4.4, 4.6 kV), and (iv) corona discharge regime (4.8 kV).

was observed at both 4.4 and 4.6 kV (Figure 4c(ii) and (iii)). However, at 4.8 kV, the emergence of corona discharge disrupted spray stability, and only a static meniscus without droplet emission was observed (Figure 4c(iv)). To confirm the stability of multi-nozzle operation, simultaneous electrospraying from the four-tip emitter was visualized using a DSLR camera equipped with a 10× magnification lens. The tips were symmetrically arranged at 90° intervals with an inter-tip spacing of ≈3 cm, as defined by the device geometry, which effectively prevents electric-field interference between adjacent nozzles. As shown in Figure S7a (Supporting Information), the four-tip emitter integrated with a ring extractor was operated at 4.6 kV. Figure S7b (Supporting Information) shows concurrent Taylor-cone formation at all four tips, demonstrating stable and independent cone-jet water electrospray.

To further quantify the electrospray behavior, the volumetric flow rate was estimated using the scaling law proposed by Chen and Pui scaling law (2),[45] which relates the flow rate Q to the jet

radius, r_j electrical conductivity K, vacuum permittivity ε_0 , and relative permittivity κ:

$$Q = \frac{\pi^2 K r_j^3}{\varepsilon_0 \kappa^{1/2}} \quad (3)$$

Based on the observed jet diameter of 3–4 µm (r_j = 1.5 – 2.0µm), the measured electrical conductivity of distilled DI water (K = 0.103 mS m^{-1}, the vacuum permittivity (ε_0 = 8.85 × 10^{-12} F m^{-1}), and the relative permittivity of water (k = 80), the volumetric flow rate was calculated to be in the range of 0.16–0.37 ml h^{-1}. This result confirms ultra-low flow rate operation consistent with the characteristics of the cone-jet mode. These findings collectively demonstrate that the proposed PPM-NFM emitter achieves stable cone-jet water electrospray without corona discharge at voltages below 5 kV, enabled by the synergistic effects of capillary-driven water delivery and electric field focusing via the ring extractor.

2.4. Evaluation of Air Purification Performance in a Sealed Chamber

The air purification performance of the proposed electrospray-based air purification device (Figure 1) was evaluated in a 0.1 m^3 sealed chamber under controlled conditions (**Figure 5a**). Particulate matter (PM) was generated using incense combustion for the standard case. To evaluate the device under different particle types, salt and oil aerosols were generated using a piezo-atomizer with 9 wt.% NaCl and 20 wt.% glycerol–water solutions, respectively. Figure S8a (Supporting Information) shows that both salt (NaCl) and oil (glycerol) aerosols were effectively removed from initial $PM_{1.0}$ concentrations of ≈1500 µg m^{-3} to below 1 µg m^{-3} within 15 min, confirming the broad applicability of the water electrospray process to diverse aerosol types. In the incense combustion test, formaldehyde (HCHO) concentration decreased from 44 to 19 µg m^{-3} within 26 min when the device was activated, whereas the fan-only operation required 44 min to reach the same level (Figure S8b, Supporting Information). In all cases, the initial $PM_{1.0}$ concentration was adjusted to ≈1500 µg m^{-3}. After the particle source was turned off, the device was immediately activated to initiate purification. $PM_{1.0}$, $PM_{2.5}$, PM_{10}, ozone, temperature, and relative humidity (RH) were continuously monitored at 1-min intervals using commercial sensors, whereas $PM_{0.3}$ was manually measured with an optical particle counter (OPC) for 2 min in each sampling. The device was operated at applied voltages ranging from 3.8 to 4.8 kV, and the airflow rate of the integrated axial fan (14–88 Cubic Feet per Minute, CFM) was systematically varied to evaluate the effect of flow velocity on particle removal efficiency. For reference, a control test was conducted with the high voltage turned off while keeping the fan on to isolate the effect of electrospray and ensure uniform particle dispersion inside the chamber.

As shown in Figure 5b, clear particulate deposition appeared on the grounded collector, and SEM confirmed microscale particulates. Figure 5c shows the time-dependent decay of $PM_{1.0}$ concentration at different voltages (3.6–4.6 kV) under a fixed airflow rate of 14 CFM. The removal rate increased with applied voltage, showing a rapid initial decline that gradually stabilized. At 4.6 kV, the $PM_{1.0}$ level decreased from ≈1500 µg m^{-3} to below 1 µg m^{-3} within 30 min. $PM_{2.5}$ and PM_{10} concentrations were measured simultaneously under the same conditions (Figure S9, Supporting Information), showing similar decay behavior to $PM_{1.0}$, and both were nearly completely removed within 30 min at 4.6 kV. Figure 5d compares the effect of airflow rate (14–88 CFM) at 4.6 kV. Increasing airflow up to 62 CFM enhanced particle transport and accelerated removal, demonstrating efficient electrostatic collection under moderate flow conditions. However, at excessively high airflow (88 CFM), the difference in removal efficiency became negligible, suggesting that some particles may bypass the collection region without being collected, leading to a slight decrease in performance. Based on these results, the applied voltage and airflow rate were fixed at 4.6 kV and 26 CFM, respectively, for subsequent PM removal experiments. Figure 5e explores the effect of humidity, where each experiment was conducted under different initial RH conditions ranging from 43% to 81%, which were set by misting DI water with a piezo atomizer. In addition, Figure S10 (Supporting Information) compares the effect of water electrical conductivity using deionized (0.103 mS m^{-1}), purified (23.0 mS m^{-1}), and tap water (33.5 mS m^{-1}). All cases achieved almost complete particle removal within 20 min, although a slight delay was observed for liquids with higher electrical conductivity. This behavior likely arises from faster charge dissipation in more conductive solutions, which destabilizes the cone-jet formation.[15]

Figure 5f shows that ozone concentrations remained below 20 ppb at all applied voltages, confirming the ozone-free operation of the device. In contrast, control tests using a dry PPM-NFM emitter exhibited a noticeable increase in ozone concentration at 4.4 and 4.6 kV, measured over 1 h of operation (Figure S11a, Supporting Information). This increase is likely associated with localized electric-field intensification at the exposed conductive ITO region near the dry tip, which can facilitate corona discharge and subsequent ozone generation. Conversely, the wet tip forms a stable Taylor-cone that increases the curvature radius and moderates the local field, while the charged water microdroplets generated during cone-jet water electrospray may further alleviate the field through a space-charge effect,[46] thereby suppressing corona discharge (Figure S11b, Supporting Information).

Figure 5g shows the long-term reproducibility of the device, where two independently fabricated modules were tested under identical conditions for more than 30 consecutive operation cycles. The removal efficiencies, calculated from 5-min averages based on PM concentration changes between 3 and 8 min after device activation, remained consistent throughout the repeated experiments, confirming stable and durable performance. The average reductions were 97.9% for $PM_{0.3}$, 85.7% for $PM_{1.0}$, 94.5% for $PM_{2.5}$, and 94.7% for PM_{10}. The high efficiency for $PM_{0.3}$ indicates effective electrostatic capture of submicron particles by charged water microdroplets, whereas the relatively lower efficiency for $PM_{1.0}$ may reflect the U-shaped trend reported for electrostatic systems, which has been attributed to the differing dominance of electrostatic attraction for smaller particles and inertial impaction for larger ones, leaving intermediate-sized particles less efficiently collected.[47] The ambient temperature was maintained between 23.5 and 25.5 °C. While RH varied slightly during each experiment, the average RH measured before and after device operation across the 30 repeated tests was 45.1% and

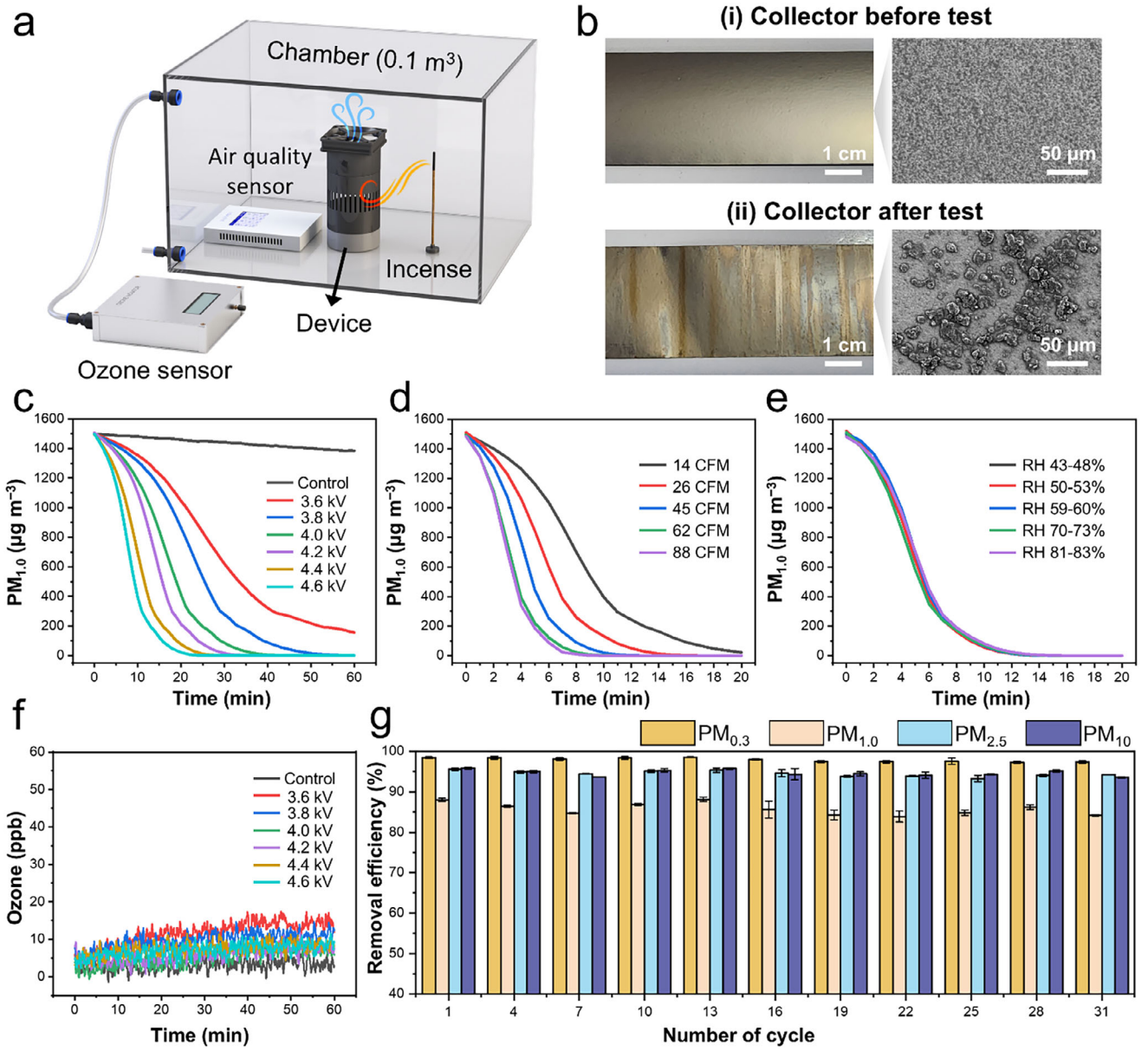

Figure 5. Air purification performance of the water electrospray device in a sealed chamber. a) Experimental setup. b) Particle deposition on the collector (i) before and (ii) after. c–e) $PM_{1.0}$ removal trends under different voltages (c), airflow rates (d), and relative humidities (e). f) Ozone concentration. g) Removal efficiency by particle size over 30 cycles; data represent mean ± SD (n = 2).

49.9%, respectively, indicating a modest overall increase. This ≈5% increase in humidity is attributed to a combination of natural evaporation from the device's water reservoir and the partial vaporization of water microdroplets generated during electrospray. Extended experiments further confirmed the durability of the device. As shown in Figure S12 (Supporting Information), the $PM_{1.0}$ removal profiles measured after 0, 12, 25, and 50 h of continuous operation were nearly identical, demonstrating stable performance without noticeable degradation. Collectively, these results demonstrate that the proposed water electrospray-based air purification device provides consistent, efficient, and ozone-free particulate removal under realistic indoor conditions, with minimal impact on temperature and humidity. These characteristics highlight its suitability for safe, sustainable operation in enclosed environments.

3. Conclusion

In this study, we developed a compact, filterless air purification device that employs ozone-free cone-jet water electrospray, driven by a self-pumped hygroscopic nanofiber-based emitter. The PPM(PVA-PAA-MMT)-NFM emitter incorporates an electrospun organic–inorganic composite composed of PVA, PAA, and MMT, which facilitates capillary-driven water transport and maintains structural integrity through thermal crosslinking. Performance evaluation was conducted in a 0.1 m^3 sealed chamber

using incense combustion as the particle source and real-time sensors for monitoring. Under an applied voltage of 4.6 kV, the device reduced $PM_{1.0}$ concentrations from ≈1500 μg m^{-3} to below 1 μg m^{-3} within 20 min. Notably, even for $PM_{0.3}$ particles that are typically difficult to remove, the device achieved over 97% reduction within the initial 5 min, which is highly encouraging. These results were consistently reproduced over 30 consecutive operation cycles and across different airflow rates and humidity conditions, confirming the robust and long-term stability of the passive PPM-NFM emitter design. Water consumption remained below 0.4 mL h^{-1} per emitter tip, and ozone levels stayed under 20 ppb. This work demonstrates the potential of nanostructured hygroscopic PPM-NFM as a foundation for scalable water electrospray-based air purification systems. By integrating material engineering, passive fluid transport, and electric field optimization, the proposed approach offers a safe, energy-efficient, and sustainable alternative to conventional filtration or corona-based methods. In particular, the incorporation of MMT into the organic polymer matrix endows the PPM-NFM with enhanced mechanical durability and structural stability, which are critical for maintaining self-pumped functionality during long-term operation. Future developments may extend their functionality to volatile organic compound removal, antimicrobial activity, and adaptive humidity control for various indoor environments, including residential, industrial, and vehicular settings.

4. Experimental Section

Materials: Poly(vinyl alcohol) (PVA, polymerization degree ≈1500) was sourced from FUJIFILM Wako Pure Chemical Corporation (Osaka, Japan; Cat. No. 160–03055) and used without further purification. Poly(acrylic acid) (PAA, average molecular weight ≈100 000) was obtained from Sigma–Aldrich Korea and employed as received. Natural sodium MMT (Na^+-MMT, commercial name: Kunipia-F), with a cation exchange capacity (CEC) of 1.15 meq g^{-1}, was supplied by Kunimine Industries, Japan. All aqueous preparations and processing steps were carried out using deionized (DI) water with a resistivity of 18.2 MΩ·cm at ambient temperature. A multilayer electrospray emitter was constructed using a flexible substrate comprising copper (Cu) foil (≈18 μm), polyimide (PI) film (≈25 μm), hot melt adhesive (≈10 μm), and electroless-plated nickel (Ni, ≈2 μm), provided in an FPCB format by TM-Tech Co., Korea. A polyimide (PI) spacer film with a thickness of 300 μm was laser-cut and laminated to define the microchannel geometry. An indium tin oxide (ITO)-coated polyethylene terephthalate (PET) film with a surface resistance of 150 Ω·sq^{-1}, a base thickness of 125 μm, was obtained from EOTech Co., Korea, and used as the conductive substrate for nanofiber deposition. A hydrophilic PET film with a thickness of 100 μm (Model No. 9901P) was purchased from AS ONE, Japan, and employed as the top sealing layer. For aerosol generation experiments, analytical-grade sodium chloride (NaCl, 99.5%, GR grade, CAS No. 7647-14-5, molecular weight = 58.45) was purchased from OCI Co., Ltd., Korea. Glycerol (99.7%, JKY Company, Korea) was used to prepare the oil aerosol solution.

Fabrication of PPM-NFM and PPM Film: The electrospinning solution for the PPM-NFM was prepared as follows. PVA and PAA were mixed at a weight ratio of 7:3, and MMT was incorporated at 3 wt.% relative to the total weight of the copolymer. To formulate a 10 wt.% spinning solution, the components were dissolved in DI water. MMT was first dispersed in DI water and treated with ultrasonication for 15 min to ensure uniform dispersion. Following this, PVA was added and stirred until fully dissolved. PAA, in liquid form, was then introduced without additional pretreatment and stirred thoroughly until a homogeneous and stable solution was obtained. All procedures were carried out at room temperature, and the solution was used immediately to avoid premature gelation. The solution was loaded into a syringe and electrospun at a flow rate of 3 μL min^{-1} under an applied voltage of 12 kV. The distance between the needle tip and the collector was fixed at 15 cm, and the process was conducted at ambient temperature. The electrospun nanofibers were collected directly onto an ITO-coated PET film with dimensions of 5 × 10 cm^2. To ensure uniform fiber deposition and prevent edge distortion, the ITO substrate was secured between rigid frames, and fibers were deposited directly onto the conductive ITO surface. This configuration was designed to facilitate seamless integration in the subsequent device assembly process. The final thickness of the PPM-NFM was 48 μm. For comparison, a control PPM film was fabricated using the same solution composition. The solution was cast onto a flat substrate by solvent casting and dried to form a film with a target thickness of 50 μm. Both the electrospun PPM-NFM and the solvent-cast PPM film, prepared on ITO-coated PET substrates, were subsequently thermally treated at 150 °C for 3 h to induce crosslinking and improve structural stability.

Water Electrospray in the Cone-jet Mode Characterization: Cone-jet water electrospray was characterized using a custom-built setup consisting of an HV power supply (+15 kV, 5 mA, Korea Switching Corp.), a grounded stainless-steel collector, and a ring extractor concentrically aligned with the emitter. The ring extractor was fabricated by laminating a copper film onto a PI substrate, followed by electroless nickel plating and precision laser cutting to define a circular aperture (inner diameter: 10 mm, outer diameter: 18 mm). The distance between the emitter tip and the collector was fixed at 10 mm. DI water (electrical conductivity: 0.103 mS m^{-1}) was manually injected using a 5 mL Luer-lock syringe and delivered to the emitter tip via capillary action through the hygroscopic nanofiber membrane. Electrospray current was measured using a picoammeter (Model 6485, Keithley Instruments Corp.), with 100 data points collected for each applied voltage (4.0–5.0 kV in 0.1 kV increments) over 25 s at a sampling rate of 4 Hz. Jet formation and spray stability were visualized using a high-speed camera (FASTCAM NOVA S6, Photron Corp.) equipped with a 10× magnification macro lens (×10-A, Nikon Corp.). A colinearly aligned LED work light (NAVI161-01, 2.88 W, NAVIMRO Corp.) was used to provide backlighting for silhouette imaging. Jet diameter was quantified from the recorded footage using ImageJ software. Figure S13a (Supporting Information) shows the experimental setup for cone-jet mode characterization of a single-tip emitter, including the fabricated ring extractor and collector. A high-speed camera with an LED backlight was used to capture real-time silhouette images of cone-jet formation. Figure S13b (Supporting Information) shows the setup for observing Taylor-cone formation from the four-tip emitter using a DSLR camera with a 10× magnification lens.

Evaluation of Air Purification Performance in a Sealed Chamber: Air purification experiments were conducted in a custom-fabricated acrylic chamber with an internal volume of ≈0.1 m^3 (36.5 × 56.5 × 47 cm^3). Particulate matter ($PM_{1.0}$, $PM_{2.5}$, PM_{10}), temperature, and relative humidity were continuously monitored using an integrated air quality sensor (AQ-SC, Kweather Corp.). Particulate matter ($PM_{0.3}$) concentration was measured using a portable optical particle counter (HT-9600, Hti Co.) with a sampling duration of 2 min per measurement. Ozone concentration was measured using an ozone sensor (HOM-6000, Himaxtech Corp.) connected outside the chamber through a hose fitting, with a sampling interval of 1 s over a 1-h period to capture real-time fluctuations. Combustion-derived aerosol particles were generated by burning commercially available household incense sticks. To control the airflow rate, commercial brushless DC cooling fans with different volumetric flow rates (14, 26, 45, 62, and 88 CFM) were mounted on the device. Additional aerosol tests were performed using a piezoelectric atomizer (JKE-20, JKC EMC Corp.) to generate salt (NaCl) and oil (glycerol) particles. The electrical conductivity of the working fluids (DI water, purified water, and tap water) was measured using a handheld pure-water conductivity meter (CM-31PW, TOADKK Corp.) to evaluate the influence of conductivity on purification performance. Surface analysis of the collector before and after purification tests was performed using a scanning electron microscope (SU5000, Hitachi Corp.). Figure S14a (Supporting Information) presents the internal structure of the device, featuring a four-tip emitter, airflow guide, and high-voltage and ground connections integrated into a compact cylindrical housing. Figure S14b (Supporting Information) shows the experimental

setup, including the placement of the prototype inside the sealed chamber, the incense stick PM source, and the positions of the air quality and ozone sensors.

Supporting Information

Supporting Information is available from the Wiley Online Library or from the author.

Acknowledgements

This work was supported by the National Research Foundation of Korea (NRF) grant funded by the Korea government (MSIT) (No. RS-2024-00435493).

Conflict of Interest

The authors declare no competing interests.

Author Contributions

J.C. and Y.C. contributed equally to this work. J.C. and Y.C. co-conceived the concept of this project and prepared the manuscript. J.Y., S.W., S.A., and J.-Y.C. conducted the literature search, organized information, and contributed to conceptualization. C.A., M.S., and E.S. created the visualizations and schematic illustrations. All authors reviewed and edited the manuscript. S.L. and I.D.K. supervised the project and approved the final manuscript.

Data Availability Statement

The data that support the findings of this study are available from the corresponding author upon reasonable request.

Keywords

filterless air purification, hygroscopic materials, organic–inorganic composite nanofiber membrane, ozone-free, water electrospray

Received: September 4, 2025
Revised: October 24, 2025
Published online:

[1] T. Z. Maung, J. E. Bishop, E. Holt, A. M. Turner, C. Pfrang, *Int. J. Environ. Res. Public Health* **2022**, *19*, 8752.
[2] D. E. Schraufnagel, J. R. Balmes, C. T. Cowl, S. De Matteis, S. H. Jung, K. Mortimer, R. Perez-Padilla, M. B. Rice, H. Riojas-Rodriguez, A. Sood, G. D. Thurston, T. To, A. Vanker, D. J. Wuebbles, *Chest* **2019**, *155*, 409.
[3] D. Thomas, P. Contal, V. Renaudin, P. Penicot, D. Leclerc, J. Vendel, *J. Aerosol Sci.* **1999**, *30*, 235.
[4] S. Bourrous, L. Bouilloux, F. X. Ouf, P. Lemaitre, P. Nerisson, D. Thomas, J. C. Appert-Collin, *Powder Technol.* **2016**, *289*, 109.
[5] A. Zukeran, P. C. Looy, A. Chakrabarti, A. A. Berezin, S. Jayaram, J. D. Cross, T. Ito, J. S. Chang, *IEEE Trans. Ind. Appl.* **1999**, *35*, 1184.
[6] T. Ferge, J. Maguhn, H. Felber, R. Zimmermann, *Environ. Sci. Technol.* **2004**, *38*, 1545.
[7] H. X. Liu, S. Y. Luo, L. Y. Yu, H. B. Zhao, J. Liang, Y. Guo, Y. Cui, S. K. Shan, X. W. Liu, J. G. Li, *Separations* **2023**, *10*, 536.
[8] D. P. Pan, C. H. Gu, D. P. Zhang, F. Zeng, *Energy Fuels* **2019**, *33*, 7813.
[9] B. B. Wu, H. Z. Tian, Y. Hao, S. H. Liu, X. Y. Liu, W. Liu, X. X. Bai, W. Z. Liang, S. M. Lin, Y. M. Wu, P. Y. Shao, H. J. Liu, C. Y. Zhu, *Environ. Sci. Technol.* **2018**, *52*, 14015.
[10] Y. Ehara, D. Yagishita, T. Yamamoto, A. Zukeran, K. Yasumoto, *Electrost. Precip.* **2009**, 670.
[11] C. J. Weschler, *Environ. Health Perspect.* **2006**, *114*, 1489.
[12] G. Tepper, R. Kessick, D. Pestov, *J. Appl. Phys.* **2007**, *102*, 113305.
[13] G. Tepper, R. Kessick, *J. Aerosol Sci.* **2008**, *39*, 609.
[14] J. H. Kim, H. S. Lee, H. H. Kim, A. Ogata, *J. Electrost.* **2010**, *68*, 305.
[15] Z. T. Wang, Y. Z. Chen, J. Y. Xue, B. Li, J. Wang, Q. M. Dong, *Phys. Fluids* **2024**, *36*, 111304.
[16] A. M. Gañán-Calvo, J. M. López-Herrera, M. A. Herrada, A. Ramos, J. M. Montanero, *J. Aerosol Sci.* **2018**, *125*, 32.
[17] Y. Kim, S. J. Lee, J. G. Hong, *ACS Omega* **2022**, *7*, 28667.
[18] N. Vaze, G. Pyrgiotakis, J. McDevitt, L. Mena, A. Melo, A. Bedugnis, L. Kobzik, M. Eleftheriadou, P. Demokritou, *Nanomedicine* **2019**, *18*, 234.
[19] M. Yasugi, Y. Komura, Y. Ishigami, *J. Nanopart. Res.* **2022**, *24*, 99.
[20] E. Tian, J. Liu, Y. Gao, J. Mo, S. Zhang, X. Bai, K. Liu, G. Xu, K. Liu, *Carbon Neutralization* **2023**, *2*, 245.
[21] A. Jaworek, A. Krupa, *J. Aerosol Sci.* **1999**, *30*, 873.
[22] J. M. López-Herrera, A. Barrero, A. Boucard, I. G. Loscertales, M. Márquez, *J Am Soc Mass Spectrom* **2004**, *15*, 253.
[23] A. Ieta, J. Primrose, D. Quill, M. Chirita, *J. Electrost.* **2011**, *69*, 461.
[24] M. R. Morad, A. Rajabi, M. Razavi, S. R. P. Sereshkeh, *Sci. Rep.* **2016**, *6*, 38509.
[25] J. H. Jeong, H. Choi, K. Park, H. Kim, J. Choi, I. Park, S. S. Lee, *Polymer* **2020**, *194*, 122405.
[26] S. Dandavino, C. Ataman, C. N. Ryan, S. Chakraborty, D. Courtney, J. P. W. Stark, H. Shea, *J. Micromech. Microeng.* **2014**, *24*, 075011.
[27] Y. C. Seo, I. You, I. Park, S. S. Kim, H. Lee, *Chem. Mater.* **2016**, *28*, 7990.
[28] X. Y. Zhao, C. Li, W. W. Yang, W. W. Deng, *J. Aerosol Sci.* **2017**, *113*, 108.
[29] Y. Wang, E. Tian, J. Liu, Y. Gao, J. Mo, S. Zhang, X. Bai, K. Liu, G. Xu, K. Liu, *Chin. J. Chem.* **2025**, *43*, 2979.
[30] Y. J. Cho, Y. Son, J. Ahn, H. Lim, S. Ahn, J. Y. Lee, P. K. Bae, I. Kim, *ACS Nano* **2022**, *16*, 19451.
[31] Y. Meng, K. H. Lou, R. Qi, Z. D. Guo, B. Shin, G. X. Liu, F. K. Shan, *ACS. Appl. Mater. Interfaces* **2018**, *10*, 20703.
[32] J. X. Chen, J. Z. Mai, C. Wang, Y. Y. Lin, D. Y. Miao, Y. Q. Lin, A. A. Babar, X. F. Wang, J. Y. Yu, B. Ding, *ACS Appl. Mater. Interfaces* **2022**, *14*, 1983.
[33] K. Kumeta, I. Nagashima, S. Matsui, K. Mizoguchi, *J. Appl. Polym. Sci.* **2003**, *90*, 2420.
[34] K. W. Kim, H. Kim, J. Choi, S. J. Choi, K. R. Yoon, *Energy Storage Mater.* **2024**, *71*, 103594.
[35] E. Rynkowska, K. Fatyeyeva, S. Marais, J. Kujawa, W. Kujawski, *Polymers* **2019**, *11*, 1799.
[36] E. S. Lee, D. Lei, K. Devarayan, B. S. Kim, *Compos. Sci. Technol.* **2015**, *110*, 111.
[37] S. L. Bee, M. A. A. Abdullah, S. T. Bee, L. T. Sin, A. R. Rahmat, *Prog. Polym. Sci.* **2018**, *85*, 57.
[38] K. G. Bhattacharyya, S. S. Gupta, *Adv. Colloid Interface* **2008**, *140*, 114.
[39] F. Uddin, *Metall. Mater. Trans. A* **2008**, *39*, 2804.
[40] T. Q. Liu, X. Peng, Y. Y. Chen, J. N. Zhang, C. Jiao, H. L. Wang, *Polym. Chem.* **2020**, *11*, 4787.
[41] A. Kapourani, K. Chachlioutaki, E. G. Andriotis, D. G. Fatouros, P. Barmpalexis, *J. Drug Delivery Sci. Technol.* **2023**, *79*, 104030.
[42] F. S. Wang, T. F. Wang, H. H. Lu, W. S. Ao-Ieong, J. E. Wang, H. L. Chen, C. H. Peng, *Macromolecules* **2017**, *50*, 6054.

[43] S. S. Ray, M. Okamoto, *Prog. Polym. Sci.* **2003**, *28*, 1539.
[44] A. Firmanda, F. Fahma, K. Syamsu, S. Suprihatin, R. Purnawati, M. Mahardika, L. Suryanegara, Y. Saito, K. Wood, R. Sinaga, *J. Environ. Chem. Eng.* **2023**, *11*, 110359.
[45] D. R. Chen, D. Y. H. Pui, *Aerosol Sci. Technol.* **1997**, *27*, 367.
[46] F. J. Higuera, *J.Fluid Mech.* **2016**, *801*, 130.
[47] M. C. Jena, S. K. Mishra, H. S. Moharana, *Aerosol Sci. Eng.* **2019**, *3*, 75.